Acta Materialia 232 (2022) 117930

Contents lists available at ScienceDirect

# Acta Materialia

journal homepage: www.elsevier.com/locate/actamat

# Synergistically enhanced thermoelectric properties in *n*-type $Bi_6Cu_2Se_4O_6$ through inducing resonant levels

HPSTAR 1609-2022

Junqing Zheng[a], Tao Hong[a], Dongyang Wang[a,*], Bingchao Qin[a], Xiang Gao[b], Li-Dong Zhao[a,*]

[a] *School of Materials Science and Engineering, Beihang University, Beijing 100191, China*
[b] *Center for High Pressure Science and Technology Advanced Research (HPSTAR), Beijing 100094, China*

A R T I C L E   I N F O

*Article history:*
Received 9 February 2022
Revised 1 April 2022
Accepted 6 April 2022
Available online 7 April 2022

*Keywords:*
Thermoelectric
$Bi_6Cu_2Se_4O_6$
Resonant levels
Electrical transport properties

A B S T R A C T

Oxygen-containing semiconductors are considered to be promising thermoelectric materials because of the high physicochemical stability. New layered oxyselenide $Bi_6Cu_2Se_4O_6$ possesses intrinsic low lattice thermal conductivity and can be modulated to *n*-type semiconductor through halogen doping, which is considered as a potential *n*-type thermoelectric oxide. In this work, first-principles calculations are utilized to obtain the electronic and phonon band structures for deeply recognizing the transport features of intrinsic $Bi_6Cu_2Se_4O_6$. Furthermore, Nb is selected as donor dopant in $Bi_6Cu_2Se_{3.6}Cl_{0.4}O_6$, realizing a significantly improved power factor of $\sim 4.3\ \mu V\ cm^{-1}\ K^{-2}$, which originates from the simultaneously optimized carrier concentration by effective doping and strengthened effective mass by inducing resonant levels around Fermi level. Meanwhile, the enhancement of phonon scattering are introduced, leading to a low lattice thermal conductivity of $\sim 0.68\ W\ m^{-1}\ K^{-1}$. Finally, thanks to the effective doping of Nb and the introduction of resonant levels, a maximum $ZT \sim 0.4$ at 873 K and an average $ZT \sim 0.21$ from 303 to 873 K can be obtained in *n*-type $Bi_{5.91}Nb_{0.09}Cu_2Se_{3.6}Cl_{0.4}O_6$. This study broadens the applicability of resonant levels to optimize performances of thermoelectric oxides, and promotes the potential application of *n*-type $Bi_6Cu_2Se_4O_6$-based thermoelectric materials in medium temperature range.


## 1. Introduction

Thermoelectric (TE) technology has been regarded as a promising method to cope with the current energy crisis and environmental pollution through converting waste heat into electric power directly and reversely [1–3]. However, its widespread application is limited by the relatively poor conversion efficiency. The performance of thermoelectric materials is appraised by the dimensionless figure of merit *ZT* defined as $ZT = (\sigma S^2 T)/\kappa$, which derives from electrical conductivity ($\sigma$), Seebeck coefficient ($S$), thermal conductivity ($\kappa$) and absolute temperature ($T$) [4–6]. Therefore, to acquire larger *ZT*, various strategies are designed to improve electrical transport properties including electrical conductivity and Seebeck coefficient, or to reduce thermal conductivity.

Compared with progressive TE alloys, which usually contain toxic or expensive metal elements such as lead [7–9]/tellurium [10–12]/antimony [13–15], oxide-based semiconductors are composed of earth-abundant, nontoxic and nonvolatile elements, which have the high physicochemical stability at high temperature [2,16–18]. Therefore, they are considered as potential TE candidates for practical applications. However, the *ZT* values of TE oxides, such as $SrTiO_3$ [19], $Ca_3Co_4O_9$ [20,21], ZnO [22], $In_2O_3$ [23,24], et al. are still unsatisfactory because of the ordinary electrical conductivity $\sigma$ ($\sim$ 100–200 S $cm^{-1}$) and relatively high thermal conductivity $\kappa$ ($\sim$ 2–10 W $m^{-1}$ $K^{-1}$). *P*-type layered oxyselenide, i.e. BiCuSeO, exhibits extremely low intrinsic thermal conductivity ($\sim$ 0.4 W $m^{-1}$ $K^{-1}$ at 923 K) and adjustable electrical conductivity [2,16]. After optimization, the peak *ZT* value was obtained in Pb and Ca dual-doped sample ($\sim$ 1.5 at 873 K) [25]. However, researches and attempts on *n*-type BiCuSeO were still unsatisfactory because stable *n*-type transport properties over the whole temperature range have not been obtained [26,27]. Most recently, by intercalating BiCuSeO with another oxyselenide $Bi_2O_2Se$, a new intercalation compound $Bi_6Cu_2Se_4O_6$ was successfully synthesized [28]. In previous work, stable *n*-type transport properties have been realized in $Bi_6Cu_2Se_4O_6$ by doping halogen at Se sites [29], and the peak *ZT* value was further enhanced to $\sim$ 0.16 at 873 K through doping transition metal element at Bi sites [30].

Inducing resonant level (RL), giving rise to a local distortion of the electronic density of states, is considered as an effective

* Corresponding authors.
*E-mail addresses:* wangdongyang@buaa.edu.cn (D. Wang), zhaolidong@buaa.edu.cn (L.-D. Zhao).

https://doi.org/10.1016/j.actamat.2022.117930
1359-6454/

way to optimize the thermoelectric properties of semiconductors. A prominent enhancement in Seebeck coefficient caused by RL can be observed when the chemical potential resides in this distortion due to the increased density of states (DOS) [31]. RL has its own unique advantages in optimizing thermoelectric material *ZT*: (1) this method solves the contradiction between electrical conductivity ($\sigma$) and Sebeck coefficient ($S$) caused by carrier concentration ($n$), and enhances $S$ purposefully by optimizing effective mass ($m^*$), often achieving the synergistic optimization of electric transport properties; (2) this method is independent of phonon properties, implying that improvements in *ZT* induced by reducing the lattice thermal conductivity ($\kappa_{lat}$) can work in conjunction with the RL mechanism [32]; (3) this method is relatively easy to implement compare with other band structure modification methods such as band convergence, band alignment, et al. RL has been proven to be effective in many advanced thermoelectric systems, such as Tl-doped PbTe [33–35], In-doped SnTe [36,37] and GeTe [38], Sn-doped $Bi_2Te_3$ [39] and $As_2Te_3$ [40], and half-Heusler alloys [41,42]. However, RL has never been used as a means of optimizing thermoelectric properties in thermoelectric oxides.

In this work, to deeply understand the physical properties of intrinsic $Bi_6Cu_2Se_4O_6$, first-principles calculations were conduvcted to evaluate electron and phonon transport properties based on the electronic and phonon band structures. Then, based on the previous researches [29,30], $Bi_6Cu_2Se_{3.6}Cl_{0.4}O_6$ was chosen as the matrix, and the selective transition metal element Nb was doped at Bi sites to modify the insulating $[Bi_2O_2]^{2+}$ layers. A pentavalent $Nb^{5+}$ can give two extra electrons to the matrix when it supersedes a $Bi^{3+}$. In addition, Nb atom has less electronegativity than Bi, so can easily extract electrons. Increased electron carriers push the Fermi level deeper into the conduction band, so that the electrical transports can be optimized. Moreover, Nb-substitution creates an additional resonant level around the Fermi level, which is beneficial for a larger effective mass. The multiple effects on electronic band structure from Nb-doping are schematically elucidated in Fig. 1(a). Due to the successively designed strategies mentioned above, the power factor (*PF*) at room temperature was enhanced from $\sim$ 0.03 $\mu$W cm$^{-1}$ K$^{-2}$ to $\sim$ 1.4 $\mu$W cm$^{-1}$ K$^{-2}$. Simultaneously, Nb-substitution strengthens the phonon scattering, thereby reduces lattice thermal conductivity from $\sim$ 1.14 W m$^{-1}$ K$^{-1}$ to $\sim$ 1.07 W m$^{-1}$ K$^{-1}$ at room temperature (Fig. 1(b)). Synchronously enhanced electrical and thermal transport properties contribute to a significant enhancement of quality factor ($B$) over the whole temperature range (Fig. 1(c)). Finally, the $ZT_{max}$ of $\sim$ 0.4 at 873 K and $ZT_{ave}$ of $\sim$ 0.21 from 303 K to 873 K are achieved in $Bi_{5.91}Nb_{0.09}Cu_2Se_{3.6}Cl_{0.4}O_6$, demonstrating a 450% increase compared with the Nb-free sample (Fig. 1(d)).

## 2. Experimental section

High-purity powder raw materials of $Bi_2O_3$, Bi, Cu, Se, BiOCl and $Nb_2O_5$ with stoichiometric ratio were weighted and cold pressed into pellets. The purity of each raw material along with the supplier can be found in the Supporting Information (SI). The acquired pellets were flame-sealed in silica tubes under vacuum, and slowly heated to 1023 K in 7 h and maintained for 12 h to process solid state reaction (SSR), then cooled to room temperature. The obtained products were crushed into powder and subsequently densified by spark plasma sintering (SPS-211Lx). The phases were identified by powder X-ray diffraction (PXRD) using Cu K$\alpha$ radiation. X-ray photoelectron spectroscopy (XPS) measurement was carried out with a Thermo Scientific ESCALAB 250 Xi spectrometer. The transmission electron microscopy (TEM) analysis is obtained from JEM F200 (JEOL), and scanning transmission electron microscopy (STEM) analysis is conducted using a JEM-ARM200F (JEOL) microscope working at 200 KV. The electrical conductivity and Seebeck coefficient were measured in a helium atmosphere by Cryoall CTA. The Hall coefficients were measured using Lake Shore 8400 by Van der Pauw method. The thermal diffusivity coefficient $D$ was measured by Netzsch LFA457 via the laser flash diffusivity method. Ultrasonic Pulser/Receiver Model 5900 PR was used to measure the longitudinal and transverse acoustic velocities. The electronic band structure and phonon distribution were calculated by first-principles calculations . More experimental details can be found in the SI.

## 3. Results and discussions

### 3.1. Intrinsic properties of $Bi_6Cu_2Se_4O_6$

Fig. 2(a) presents the crystal structure of $Bi_6Cu_2Se_4O_6$. Tetragonal $Bi_6Cu_2Se_4O_6$ possesses a two-dimensional layered structure with the space group *P4/nmm*. It can be regarded as an intercalated compound formed by alternating stacking of BiCuSeO and $Bi_2O_2Se$ in a ratio of 1:2. Similar like BiCuSeO and $Bi_2O_2Se$, the insulating $[Bi_2O_2]^{2+}$ layers serve as charge reservoirs, while conductive $[Cu_2Se_2]^{2-}$/$[Se]^{2-}$ layers act as the pathway to transfer carriers [2,43]. To further understand the electrical transport properties, the electronic band structure and projected DOS of pristine $Bi_6Cu_2Se_4O_6$ was calculated via first-principles calculations and shown in Fig. 2(b). According to the electronic band structure, the valence band maximum (VBM) and the conduction band minimum (CBM) are situated along Γ-M and Γ point, suggesting that $Bi_6Cu_2Se_4O_6$ is an indirect narrow band gap ($\sim$ 0.46 eV) semiconductor, which is corresponding to previous report ($\sim$ 0.48 eV) [30]. Obviously, the CBM along Γ-Z direction is flatten, while along Γ-X direction is very sharp, indicating a strong anistropic effective mass of CBM and a excellent carrier mobility in the inplane direction. Interestingly, a sub-minimum of conduction band can be found around Z point with smaller energy above CBM around Γ point, suggesting a potential multi-band transport of electrons with suitable $n$-type doping. As observed from the projected density of states (PDOS), the conduction band is mostly contributed by Bi, and the valence band mainly originate from the rest atoms. Therefore, the conduction band can be modified by alloying other elements at Bi sites to improve $n$-type transport properties.

The crystal structure of this new compound was further probed by electron microscopy images presented in Fig. 3. The size of grains was observed by backscattered electron image (BEI, Fig. 3(a)). The grain size of the sample is roughly distributed in the range of $\sim$ 30 - 50 $\mu$m. The plate-like structure of $Bi_6Cu_2Se_4O_6$ can be obviously exhibited in the morphology image (Fig. 3(b)). As can be seen in high-resolution transmission electron microscopy (HRTEM, Fig. 3(c)), $Bi_2O_2Se$ and $Bi_2O_2Cu_2Se_2$ layers can be observed to stack alternately, which is consistent with the structure described above. The selected area electron diffraction (SAED) pattern along [100] zone axis is presented in Fig. 3(d). The typical experimental patterns indexed and well consistent with the simulated patterns shown in **Fig. S1**(c). The interlayer distance between diffraction spots is determined as 2.54 1/nm. The high-angle annular dark field scanning transmission electron microscopy (HAADF STEM) image (Fig. 3(e)) not only displays the position of atomic columns, but also provides information about local composition at atomic scale. As shown in the enlarged image (Fig. 3(f)), the visibly strong contrasts can be observed between Bi/Se and Cu/O atoms because of large differences in atomic numbers ($Z_{Bi}$ = 83, $Z_{Cu}$ = 29, $Z_{Se}$ = 34, $Z_O$ = 8). The structural model of $Bi_6Cu_2Se_4O_6$ was put in the top right corner of Fig. 3(f), and atoms in the image correspond to the structure one by one. Atomic columns are marked in Fig. 3(f) to show the alternating stacking of $[Bi_2O_2]^{2+}$, $[Cu_2Se_2]^{2-}$ and $[Se]^{2-}$ layers in strict order, further verifying the accuracy of the crystal structure discussed above. In summary, these observa-

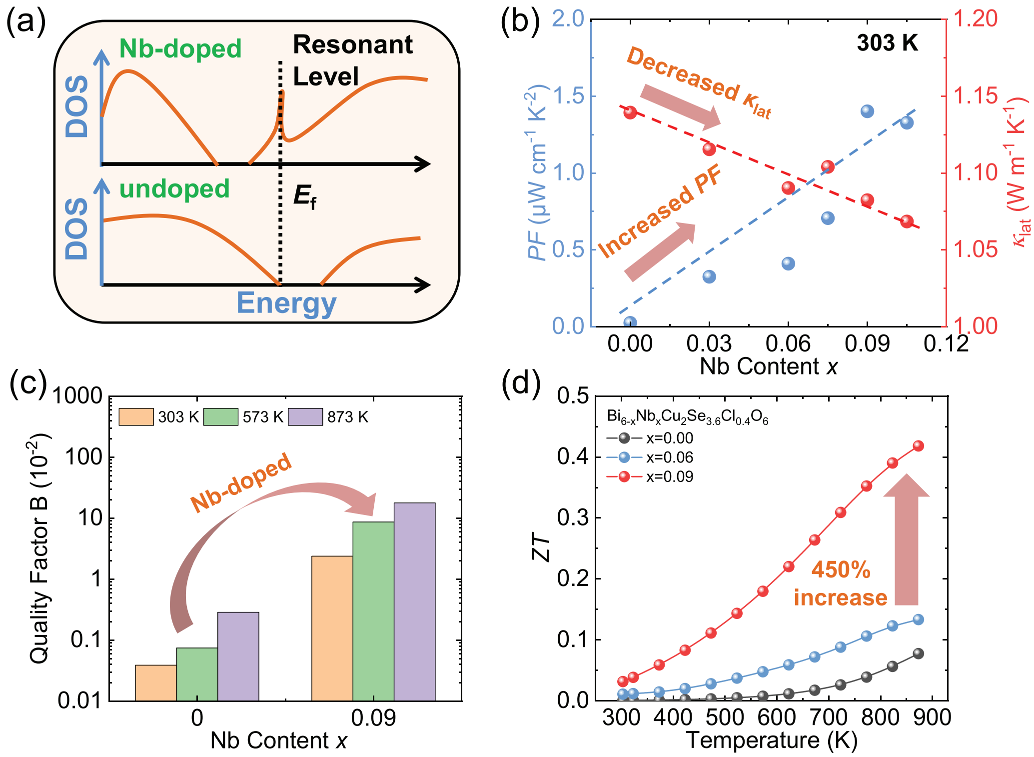


**Fig. 1.** Nb doping synergistically optimizes carrier and phonon transport properties of $Bi_6Cu_2Se_4O_6$: (a) schematic mechanisms of adjustment of density of states by Nb doping; (b) power factor (*PF*) and lattice thermal conductivity at 303 K varying with Nb content; (c) optimized quality factor (*B*) over the entire temperature range; (d) sharply enhanced *ZT* values varying with temperature.

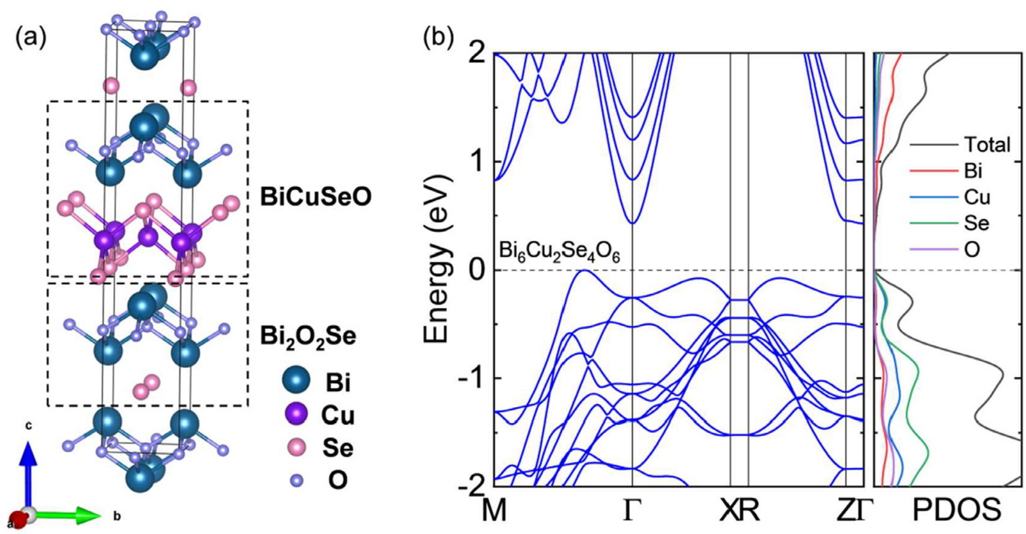


**Fig. 2.** (a) The crystal structure and (b) calculated electronic band structure and projected density of states (PDOS) of $Bi_6Cu_2Se_4O_6$.

tions from TEM are different from existing BiCuSeO and $Bi_2O_2Se$, indicating the successful synthesis of new intercalation compounds $Bi_6Cu_2Se_4O_6$.

In previous research of $Bi_6Cu_2Se_4O_6$, the relatively low intrinsic lattice thermal conductivity $\kappa_{lat}$ is noteworthy [29,30], which is believed to results from the phonon transport properties in those typical layered crystal structure. Therefore, to deeply understand the thermal transport properties of $Bi_6Cu_2Se_4O_6$, the phonon spectrum was quantified via density functional theory (DFT) calculations within the quasi-harmonic approximation. **Fig. S2**(a) presents phonon modes along the high symmetry lines of first Brillouin zone, in which optic phonon branches presented by black lines has higher frequency and the rest three are acoustic phonon branches. The corresponding atomic phonon density of states (PhDOS) are revealed in **Fig. S2**(b). As can be observed, the high frequency optic branches are mainly contributed by O, and the low frequency optic and acoustic branches mainly originate from the rest atoms. Because lattice heat conduction is dominated by the low frequency optic and acoustic phonon branches, the low frequency part of the spectrum is magnified and shown in Fig. 4(a). Obviously, the flatter phonon modes can be observed in Γ-Z direction, so the velocity (listed in Table 1) of Γ-Z direction is smaller than Γ-X direction. Moreover, The acoustic modes boundary frequency is relatively low as listed in Table 1, implying the soft modes related

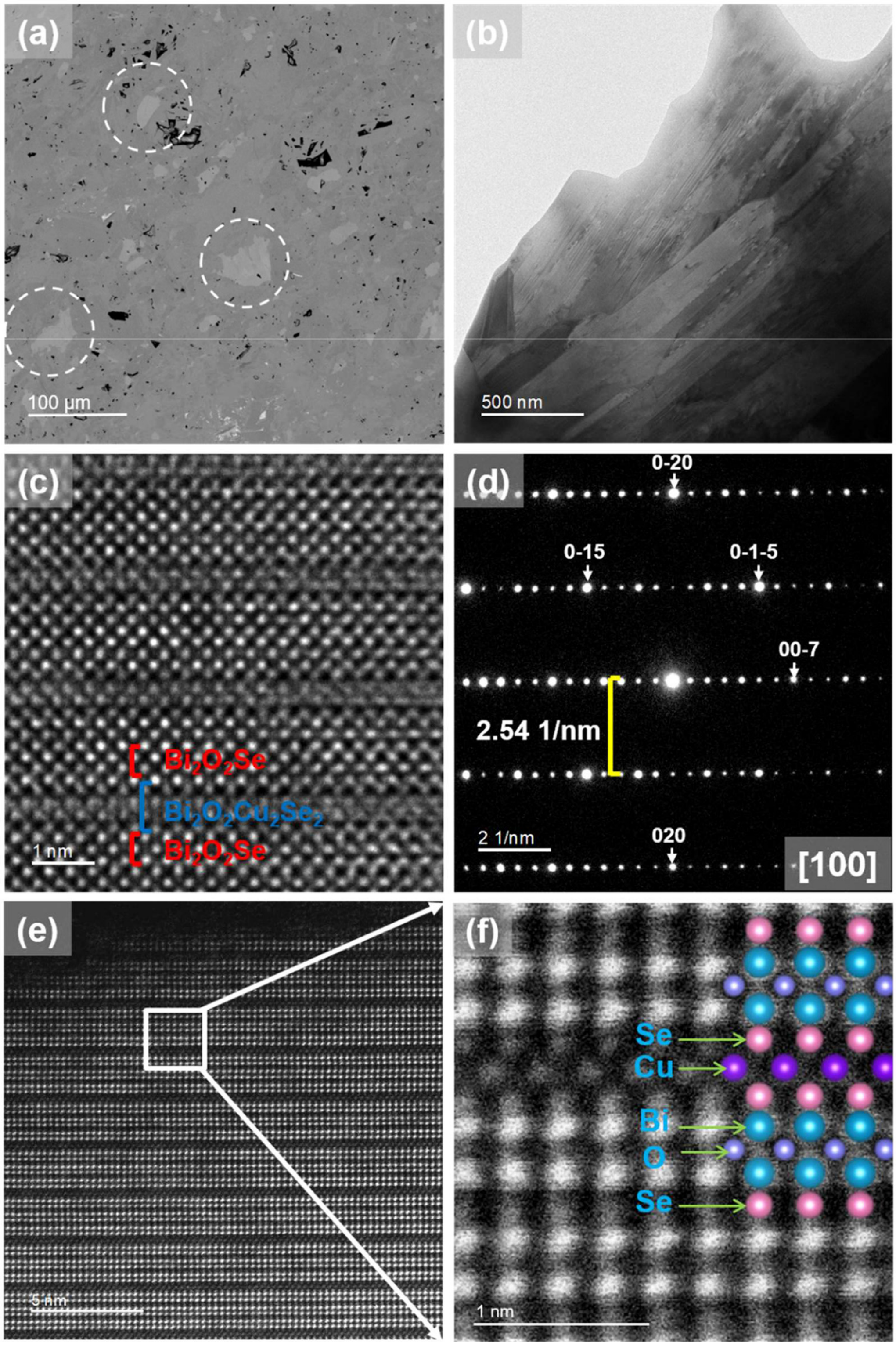


**Fig. 3.** Structural characterizations of $Bi_6Cu_2Se_4O_6$: (a) backscattered electron image, several typical grains are highlighted by white dashed squares; (b) morphology image; (c) high-resolution transmission electron microscopy image; (d) selected area electron diffraction patterns along [100] zone axis; (e) high-angle annular dark field scanning transmission electron microscopy image with (f) the enlarged one.

to weak chemical boding, low Debye temperature, and strong anharmonicity [44,45]. At Γ point, the low frequency optic branches suppress the acoustic branches resulting in the coupling between the optic and acoustic branches, thereby intensifying the phonon-phonon scattering [46–48]. The Grüneisen parameter ($\gamma$) is often used to reflect phonon vibrations in unit cell, reflecting the anharmonicity [49,50]. Accordingly, this acoustic-optic coupling leads to larger $\gamma$ in the low-frequency region (Fig. 4(b)).

To obtain the quantitative anharmonicity along different directions, the mode Grüneisen parameters are depicted in Fig. 4(c) and the averaged values can be gotten in Table 1. Consistent with the above discussion, the large $\gamma$ is obtained in both Γ-Z and Γ-X di-

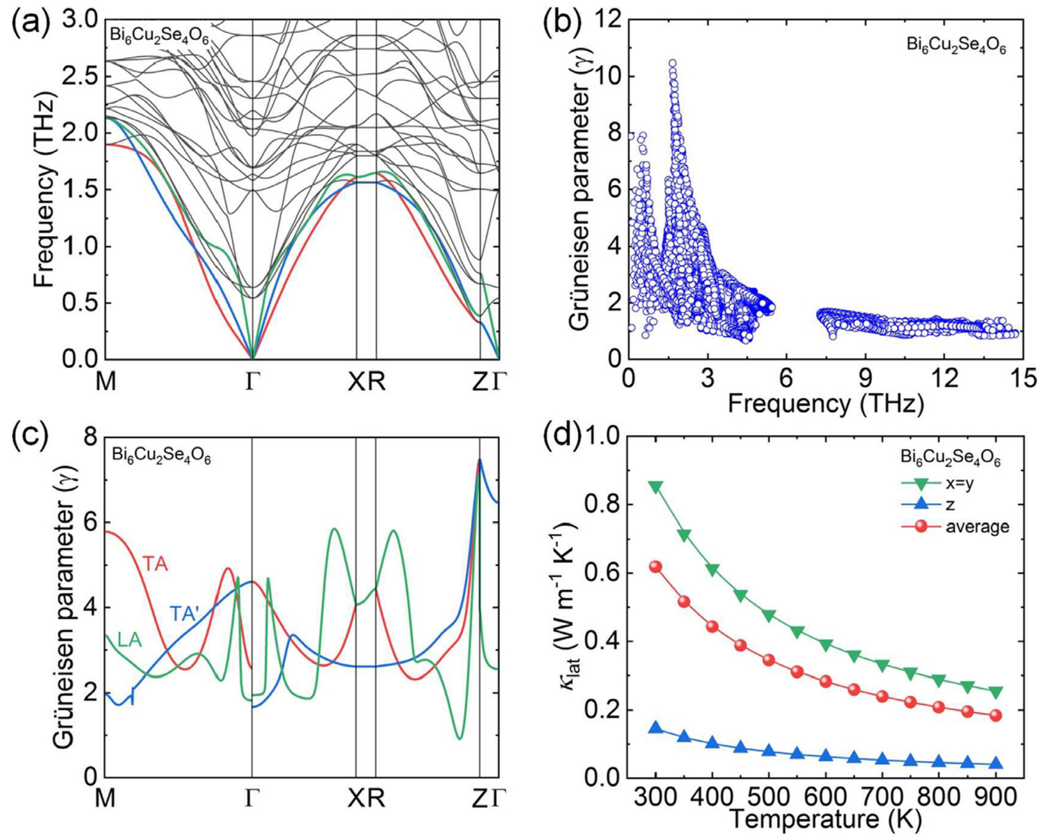


**Fig. 4.** Calculated (a) low-frequency phonon dispersion, (b) mode Grüneisen parameters, (c) Grüneisen dispersions and (d) anisotropic lattice thermal conductivity for $Bi_6Cu_2Se_4O_6$ calculated from Debye-Callaway model.

**Table 1**
The phonon group velocity, cutoff frequency and averaged Grüneisen Parameter for transverse (TA, TA') and longitudinal (LA) acoustic phonon modes along Γ-X and Γ-Z directions.

| | Velocity (m s$^{-1}$) | | Frequency (THz) | | Grüneisen Parameter | |
|---|---|---|---|---|---|---|
| | Γ-X | Γ-Z | Γ-X | Γ-Z | Γ-X | Γ-Z |
| TA | 1710 | 1635 | 1.61 | 0.33 | 3.35 | 6.82 |
| TA' | 2423 | 1635 | 1.56 | 0.33 | 2.62 | 6.82 |
| LA | 3736 | 3510 | 1.61 | 0.77 | 3.32 | 2.81 |

**Table 2**
Comparisons of theoretical and experimental elastic properties of $Bi_6Cu_2Se_4O_6$.

| | Theoretical value | Experimental value |
|---|---|---|
| Longitudinal wave velocity $v_l$ (m s$^{-1}$) | 3795 | 3693 |
| Transverse wave velocity $v_s$ (m s$^{-1}$) | 1932 | 1963 |
| Average wave velocity $v_a$ (m s$^{-1}$) | 2165 | 2193 |
| Bulk modulus $K$ (GPa) | 88.4 | 74.5 |
| Shear modulus $G$ (GPa) | 35.0 | 34.4 |
| Young modulus $E$ (GPa) | 92.8 | 89.4 |
| Poisson ratio $v_p$ | 0.32 | 0.30 |
| Grüneisen parameter $\gamma$ | 1.90 | 1.77 |
| Debye temperature $\theta_D$ (K) | 248 | 259 |

rections due to the soft modes, implying stronger anharmonicity and low lattice thermal conductivity. The theoretical and experimental elastic properties of $Bi_6Cu_2Se_4O_6$ are listed in Table 2 and present a good accordance with each other. Distinctly, $Bi_6Cu_2Se_4O_6$ possesses a small Young modulus $E$, a large Grüneisen parameter $\gamma$ and a low Debye temperature $\theta_D$, implying a low lattice thermal conductivity $\kappa_{lat}$ according to the following Eqs. (1) and (2) [47,51–53]:

$$\kappa_{lat} = \frac{3.0 \times 10^{-5}\overline{M_a}a^{1/3}\theta_D^3}{T\gamma^2 v^{2/3}} \tag{1}$$

$$\kappa_{lat} \propto \frac{\rho^{1/6}E^{1/2}}{\overline{M_a}^{2/3}} \tag{2}$$

where $\overline{M_a}$ is the mean atomic weight, $a$ is the average volume occupied by one atom, $v$ is the atoms number of the primitive cell, $\rho$ is the sample density, respectively. Finally, the $\kappa_{lat}$ varying with temperature quantificated via Debye-Callaway model is shown in Fig. 4(d). The $\kappa_{lat}$ is anisotropic, and the extremely low $\kappa_{lat}$ is obtained in both $x$-axis (~ 0.26 W m$^{-1}$ K$^{-1}$ at 900 K) and $z$-axis (~ 0.04 W m$^{-1}$ K$^{-1}$ at 900 K). The calculated average $\kappa_{lat}$ varies from ~ 0.62 W m$^{-1}$ K$^{-1}$ at 300 K to ~ 0.18 W m$^{-1}$ K$^{-1}$ at 900 K. According the above discussion, the causes of intrinsic low $\kappa_{lat}$ in $Bi_6Cu_2Se_4O_6$ can be summarized as the acoustic-optic coupling, the soft phonon modes and the strong anharmonicity in layered crystal structure.

### 3.2. Thermoelectric properties of Nb-doped $Bi_6Cu_2Se_{3.6}Cl_{0.4}O_6$

The powder XRD patterns for $Bi_{6-x}Nb_xCu_2Se_{3.6}Cl_{0.4}O_6$ ($0 \le x \le 0.105$) are presented in Fig. 5(a), and the standard card is adopted from calculation results of Rosseinsky et al. [28]. All the major peaks can be well indexed to $Bi_6Cu_2Se_4O_6$ phase, while the additional mionor peak of $Nb_2O_5$ as the secondary phase can be found in x = 0.105 sample as marked with red quadrilateral. The presence of $Nb_2O_5$ in x > 0.09 suggessts that the solubility limit of Nb in $Bi_6Cu_2Se_4O_6$ can be roughly estimated to be 1.5%. Fig. 5(b)

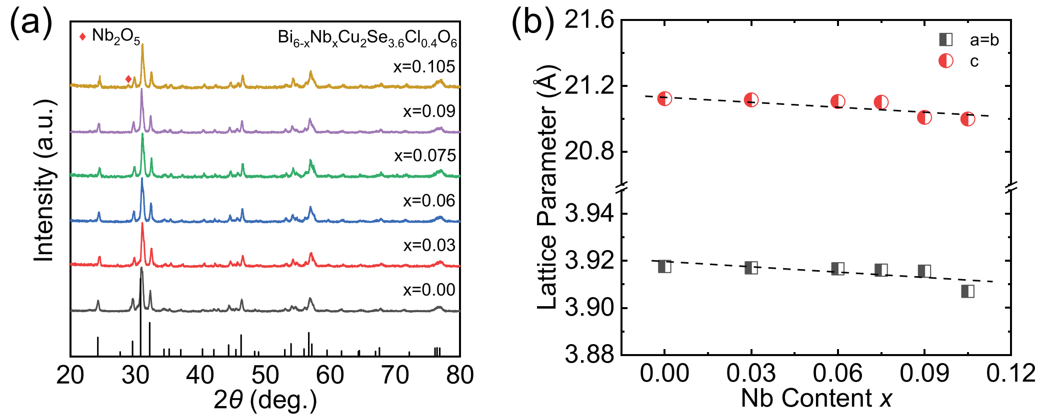


**Fig. 5.** (a) Powder XRD patterns and (b) lattice parameters of $Bi_{6-x}Nb_xCu_2Se_{3.6}Cl_{0.4}O_6$ ($0 \leq x \leq 0.105$).

shows the lattice parameters calculated according to XRD patterns varying with Nb content. All the lattice parameters presents the trend of monotonic decrease as the Nb content increases. The unit cell undergoes a regular shrinkage from x = 0 to x = 0.105, which is relavent to the smaller ionic radius of $Nb^{5+}$ (~ 0.70 Å) than $Bi^{3+}$ (~ 1.08 Å). The monotonically decreasing lattice parameters also indicate that Nb successfully enters the unit cell to substitute Bi.

The electrical transport properties of $Bi_{6-x}Nb_xCu_2Se_{3.6}Cl_{0.4}O_6$ ($0 \leq x \leq 0.105$) are displayed in Fig. 6. It should be emphasized that, according to the previous researches, the testing directions of thermoelectric properties are all along the optimal direction, namely the direction perpendicular to sintering pressure [29,30]. The comparison of thermoelectric properties measured in the directions perpendicular or parallel to sintering pressure is shown in **Fig. S3**, which proves the the correctness of optimal direction selected in this work. As shown in Fig. 6(a), small amount of Nb dopant can signally enhance the electrical conductivity ($\sigma$). The Nb-free sample exhibits semiconducting behavior with extremely low $\sigma$ from ~ 6.8 S $cm^{-1}$ at 303 K to ~ 26.8 S $cm^{-1}$ at 873 K; while Nb-doped samples exhibit degenerate semiconductor behavior, and the best $\sigma$ is obtained in $Bi_{5.91}Nb_{0.09}Cu_2Se_{3.6}Cl_{0.4}O_6$ from ~ 406 S $cm^{-1}$ at 303 K to 140 S $cm^{-1}$ at 873 K. Further increasement of Nb content has an obviously opposite effect on $\sigma$ because of the existence of $Nb_2O_5$ secondary phase. Furthermore, Nb doping can also slightly improve the Seebeck coefficient ($S$), especially in high temperature region (Fig. 6(b)). All the samples display a negtive $S$ over the entire temperature range, implying a stable $n$-type transport behavior. The $S$ value between ecah Nb-doped sample has little difference, remaining in the range of ~ 50 $\mu$V $K^{-1}$ to ~ 170 $\mu$V $K^{-1}$. The lagest $S$ value is enhanced from ~ 160 $\mu$V $K^{-1}$ in $Bi_6Cu_2Se_{3.6}Cl_{0.4}O_6$ to ~ 177 $\mu$V $K^{-1}$ in $Bi_{5.91}Nb_{0.09}Cu_2Se_{3.6}Cl_{0.4}O_6$ at 873 K. The simultaneous enhanced $\sigma$ and $S$ illustrate that Nb substitution can optimize the electrical transport properties comprehensively. On the basic of the $\sigma$ and $S$ discussed above, the power factor ($PF = \sigma S^2$) varying with temperature is depicted in Fig. 6(c). Benefiting from the obviously enhanced $\sigma$ and slightly improved $S$, the $PF$ is significantly boosted with Nb doping, from ~ 0.03 $\mu$V $cm^{-1}$ $K^{-2}$ at 303 K and ~ 0.68 $\mu$V $cm^{-1}$ $K^{-2}$ at 873 K for $Bi_6Cu_2Se_{3.6}Cl_{0.4}O_6$ to ~ 1.4 $\mu$V $cm^{-1}$ $K^{-2}$ at 303 K and ~ 4.3 $\mu$V $cm^{-1}$ $K^{-2}$ at 873 K for $Bi_{5.91}Nb_{0.09}Cu_2Se_{3.6}Cl_{0.4}O_6$.

The electrical conductivity $\sigma$ and Seebeck coefficient $S$ are two physical quantities coupled by carrier concentration $n_H$. $\sigma$ correlates with $n_H$ positively following Eq. (3), while $S$ correlates with $n$ negatively following Eq. (4) [5,54,55]:

$$\sigma = ne\mu \tag{3}$$

$$S = \frac{8\pi^2 {k_B}^2}{3eh^2} m^* T \left(\frac{\pi}{3n_H}\right)^{\frac{2}{3}} \tag{4}$$

where $e$, $\mu$, $k_B$, $h$ and $m^*$ represent unit charge, carrier mobility, Boltzmann constant, Planck constant and effective mass, respectively. In order to clarify reasons for the all-round enhancement of electrical transport performance, the relation between $S$ and $n_H$ of $Bi_{6-x}Nb_xCu_2Se_{3.6}Cl_{0.4}O_6$ ($0 \leq x \leq 0.105$) at 303 K is depicted by the Pisarenko line (Fig. 6(d)). All the experimental $S$ data points distribute above the theoretical line, implying the increasement of effective mass $m^*$. Moreover, the deduced effective mass from Eq. (4) based on the measued Hall carrier concentration ($n_H$) at 303 K are shown in the inset of Fig. 6(d). $m^*$ is optimized from ~ $0.26m_0$ to ~ $0.46m_0$ after Nb doping. When $Nb^{5+}$ is doped into $Bi^{3+}$ sites, two extra electrons would be introduced into the matrix as presented by the defect chemistry reaction:

$$Nb^{5+} \xrightarrow{Bi^{3+}} Nb_{Bi}^{\cdot\cdot} + 2e'$$

The valence states of elements in $Bi_{6-x}Nb_xCu_2Se_{3.6}Cl_{0.4}O_6$ system can be probed by X-ray photoelectron spectroscopy (XPS) [56–58]. The valence states of Bi, Cu, Se, O and Cl are analyzed in Fig. 7(a)–(e). These elements are present in the system at the expected valence states (Bi: +3, Cu: +1, Se: -2, O: -2, and Cl: +4). The high-resolution spectrum for Nb 3d exhibits two peaks at ~ 206.5 eV ($3d_{5/2}$) and ~ 209 eV ($3d_{3/2}$) as shown in Fig. 7(f). The binding energy of Nb $3d_{5/2}$ (~ 206.5 eV) is consistent with $Nb_2O_5$ [59], implying that Nb ions shows +5 valence in this system. Although part of Nb exists at 0 valence with the binding energy around ~ 200.0 eV, the substitution of $Nb^{5+}$ for $Bi^{3+}$ still contributes electrons to the matrix, causing an increase in electron carrier concentration. In addition, Nb atom has less electronegativity than Bi, so can easily extract electrons. Hence, $Nb^{5+}$ can act as an effective electron donor, and increase $n_H$ from ~ 1.8 × $10^{19}$ $cm^{-3}$ to ~ 6.2 × $10^{19}$ $cm^{-3}$ (Fig. 6(e)). Although the improved $n$ would worsen the $S$ value, Nb doping also optimizes $m^*$ to compensate for the adverse effects of inreased $n$, thereby leads to the slightly increase of $S$ [60]. The Hall mobility ($\mu_H$) can be also calculated by the measured $\sigma$ and $n_H$ following Eq. (3) [61], and displayed in Fig. 6(e) varying with Nb content. As can be seen, Nb doping increases $\mu_H$. As shown in **Fig. S4**(b), the temperature-dependent $\mu_H$ clearly reveals the carrier scattering mechanism. The exponents $x$ of -3/2, 3/2, and 1 in $\mu_H \approx T^x$ indicate that the scattering is predominantly acoustic phonon scattering, impurity ionized scattering, and vacancy scattering, respectively [62,63]. After that the vacancies were filled with Nb atoms, **Fig. S4**(b) shows that the vacancy scattering is eliminated while the acoustic phonon scattering becomes predominant. Therefore, the introduction of Nb can effectively weaken the carriers scattering by occupying the vacancy defects, thus leading to the increase of $\mu_H$.

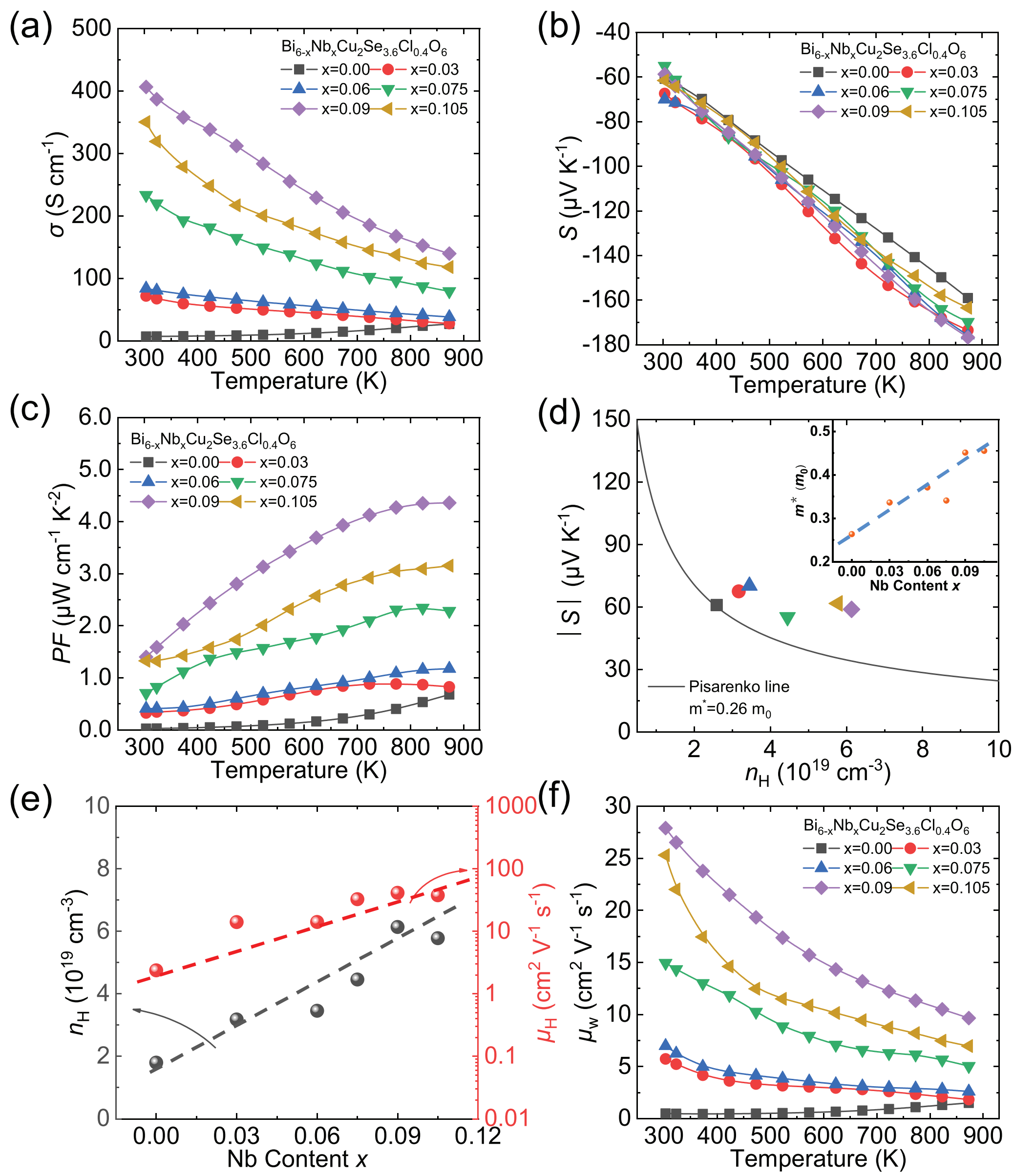

Fig. 6. Electrical transport properties of $Bi_{6-x}Nb_xCu_2Se_{3.6}Cl_{0.4}O_6$ ($0 \leq x \leq 0.105$): temperature-dependent (a) electrical conductivity, (b) Seebeck coefficient and (c) power factor; (d) Pisarenko relationship with effective mass $m^* = 0.26m_0$ at 303 K, and the inset shows $m^*$ changing with Nb content at 303 K; (e) Hall carrier concentration and mobility as a function of Nb content at 303 K; (f) temperature-dependent weighted carrier mobility.

Because both carrier concentration $n$ and effective mass $m^*$ are closely associated with carrier mobility $\mu$, weighted carrier mobility $\mu_w$ is introduced to assess the carriers transport properties Fig. 6(f)). According to measured $\sigma$ and $S$, the $\mu_w$ can be calculated by Eq. (5) to ((7) [64–67]:

$$\mu_w = \frac{3\sigma}{8\pi eF_0(\eta)}\left(\frac{h^2}{2m_e k_B T}\right)^{3/2} \tag{5}$$

$$F_n(\eta) = \int_0^\infty \frac{x^n}{1+e^{x-\eta}}dx \tag{6}$$

$$S = \pm\frac{k_B}{e}\left(\frac{(r+5/2)F_{r+3/2}(\eta)}{(r+3/2)F_{r+1/2}(\eta)} - \eta\right) \tag{7}$$

where $F_n(\eta)$, $r$, and $\eta$ denotes the Fermi integral, the scattering factor, and the reduced chemical potential, respectively. Considering the main contribution of phonon scattering, $r$ was set to -1/2. Small amount of Nb dapant can significantly enhance the $\mu_w$ over the entire temperature range. Relatively high $\mu_w$ approaching to $\sim$ 28 $cm^2\ V^{-1}\ s^{-1}$ (303 K) and $\sim$ 9.6 $cm^2\ V^{-1}\ s^{-1}$ (873 K) is obtained in $Bi_{5.91}Nb_{0.09}Cu_2Se_{3.6}Cl_{0.4}O_6$ with $n_H \sim 6.2 \times 10^{19}\ cm^{-3}$. The large increase of $\mu_w$ also marks the optimization of carrier transport properties by Nb doping.

To further explore the influence of Nb-doping on electronic band structure of $Bi_6Cu_2Se_4O_6$, the electronic band structures and density of states of $Bi_{24}Cu_8Se_{16}O_{24}$ and $Bi_{23}NbCu_8Se_{16}O_{24}$ are calculated by DFT and presented in Fig. 8. Undoped $Bi_{24}Cu_8Se_{16}O_{24}$ has a Fermi level located near VBM in forbidden band, which is consistent with its semiconductor behavior (Fig. 8(a)). After Nb substitution, the Fermi level of $Bi_{23}NbCu_8Se_{16}O_{24}$ moves up into the conduction band due to the two electrons introduced, thus exhibiting degenerate semiconductor behavior (Fig. 8(b)). Obviously, a flatten band can be found around the Fermi level, which is mainly contributed by Nb atoms. These flatten bands formed a sharp peak around Fermi level in projected density of states, resulting from the resonant levels, as shown in right panel of

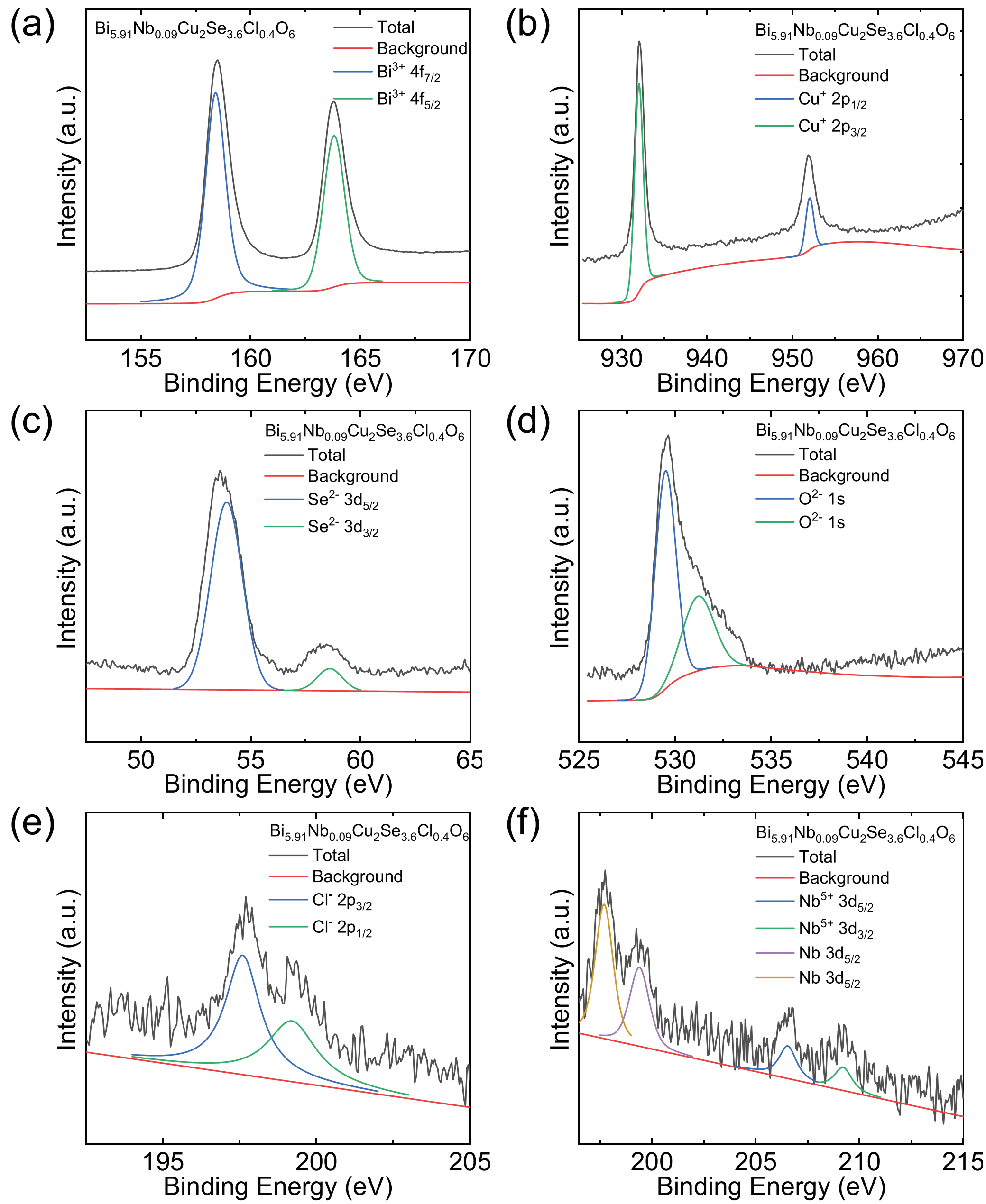


**Fig. 7.** X-ray photoelectron spectroscopy of $Bi_{5.91}Nb_{0.09}Cu_2Se_{3.6}Cl_{0.4}O_6$: (a) $Bi^{3+}$ $4f_{7/2}$ and $4f_{5/2}$ core states, (b) $Cu^+$ $2p_{3/2}$ and $2p_{1/2}$ core states, (c) $Se^{2-}$ $3d_{5/2}$ and $3d_{3/2}$ core states, (d) $O^{2-}$ 1s core states, (e) $Cl^-$ $2p_{3/2}$ and $2p_{1/2}$ core states, (f) $Nb^{5+}$ $3d_{5/2}$ and $3d_{3/2}$ core states, and Nb $3d_{5/2}$ core states.

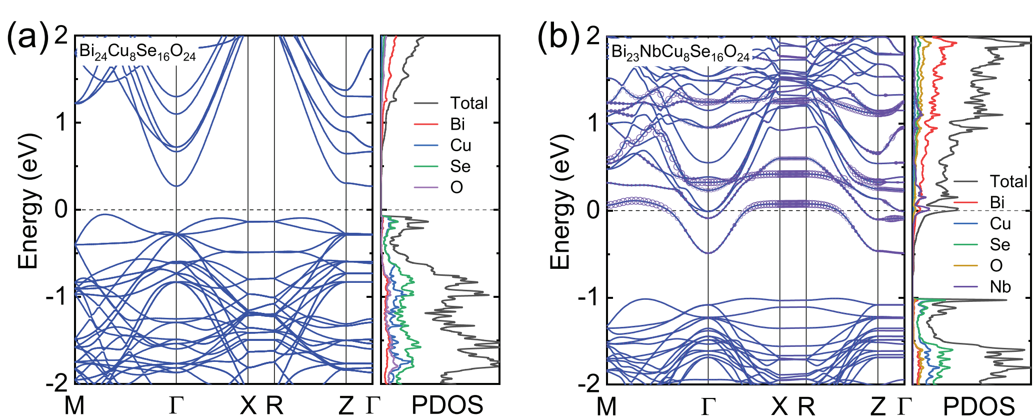


**Fig. 8.** Calculated electronic band structures and projected DOS in (a) $Bi_{24}Cu_8Se_{16}O_{24}$ and (b) $Bi_{23}NbCu_8Se_{16}O_{24}$.

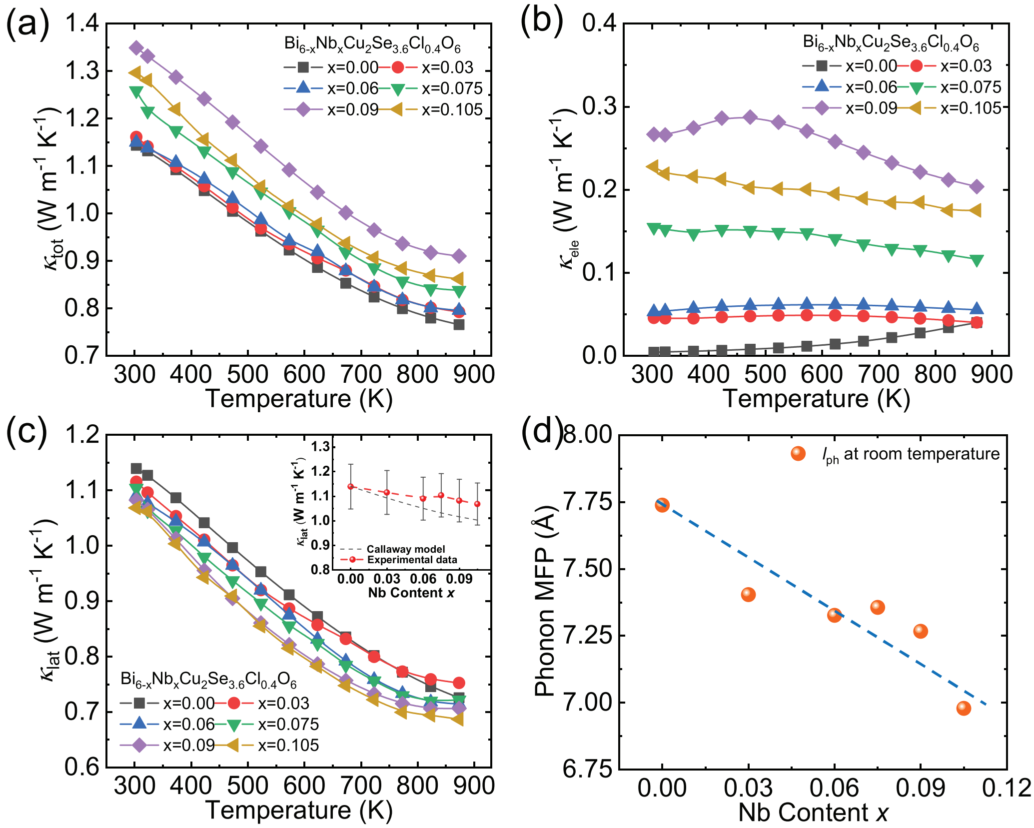


**Fig. 9.** Thermal transport properties of $Bi_{6-x}Nb_xCu_2Se_{3.6}Cl_{0.4}O_6$ ($0 \le x \le 0.105$): temperature-dependent (a) total thermal conductivity, (b) electronic thermal conductivity and (c) lattice thermal conductivity, and the inset shows lattice thermal conductivity at 303 K by experimental data and Callaway model; (d) room-temperature phonon mean free path varying with Nb content.

Fig. 8(b), which is beneficial to the Seebeck coefficient. The enhancement of Seebeck coefficient after Nb doping over the entire temperature range implies the weak temperature dependence of the resonant levels. As the results, Nb doping has double effect on the electrical properties: introducing more electrons into the matrix to optimize electrical conductivity and introducing resonant levels around the Fermi level to enlarge electron effective mass [32], thereby enhance Seebeck coefficient.

The temperature-dependent total thermal conductivity $\kappa_{tot}$ of $Bi_{6-x}Nb_xCu_2Se_{3.6}Cl_{0.4}O_6$ ($0 \le x \le 0.105$) is depicted in Fig. 9(a). The monotonously declining trend of $\kappa_{tot}$ with rising temperature suggests that phonons make a major contribution to heat conduction. $\kappa_{tot}$ firstly increases with the rising Nb dopant content, and then decreases when exceding the solubility limit due to the appearance of $Nb_2O_5$ second phase. To deeply understand the phonon transport properties, the Wiedemann–Franz law is introduced and expressed by Eqs. (8) and (9) [5]:

$$\kappa_{ele} = L\sigma T \tag{8}$$

$$\kappa_{tot} = \kappa_{lat} + \kappa_{ele} \tag{9}$$

where $L$ denotes the Lorenz number extracted by fitting the experimental $S$ values to the reduced chemical potential $\eta$, and the detailed calculation method can be found in SI. The electronic thermal conductivity $\kappa_{ele}$ varying with temperature is calculated by Eq. (8) and plotted in Fig. 9(b). There is a drastic increase in $\kappa_{ele}$ after Nb doping due to the greatly enhanced electrical conductivity $\sigma$, from ~ 0.02 W m$^{-1}$ K$^{-1}$ in $Bi_6Cu_2Se_{3.6}Cl_{0.4}O_6$ to ~ 0.28 W m$^{-1}$ K$^{-1}$ in $Bi_{5.91}Nb_{0.09}Cu_2Se_{3.6}Cl_{0.4}O_6$ at 303 K.

The lattice thermal condectivity $\kappa_{lat}$ is subsequently determined following Eq. (9) by directly subtracting $\kappa_{ele}$ from $\kappa_{tot}$. As shown in Fig. 9(c), $\kappa_{lat}$ displays a downward trend with the rising Nb content. The lowest $\kappa_{lat}$ is obtained in $Bi_{5.895}Nb_{0.105}Cu_2Se_{3.6}Cl_{0.4}O_6$ from ~ 1.06 W m$^{-1}$ K$^{-1}$ at 303 K to ~ 0.68 W m$^{-1}$ K$^{-1}$ at 873 K. This decrease is definitely attributed to the point defects of Nb substitution. As the lighter and smaller $Nb^{5+}$ enters into the $Bi^{3+}$ sites, the phonon scattering process is intensified due to the mass fluctuation and the lattice distortion. The theoretical calculations based on the Callaway model [68–70] are carried out to verify the influence of point-defect scattering on $\kappa_{lat}$, and the results are shown in the inset of Fig. 9(c). Within the scope of errors, the calculated results exhibit a good accordance with experimental data after Nb doping, indicating that Nb doping can effectively reduce $\kappa_{lat}$ by strengthening point-defect scattering. To further evaluate the influence on point defects on phonon transport, the phonon mean free path $l_{ph}$ is quantified by Eqs. (10) and (11) [52,71]:

$$v_a = \left[\frac{1}{3}\left(\frac{1}{v_l^3} + \frac{2}{v_t^2}\right)\right]^{-\frac{1}{3}} \tag{10}$$

$$\kappa_{lat} = \frac{1}{3} C_v v_a l_{ph} \tag{11}$$

Here $v_a$ represents average sound speed calculated by the longitudinal ($v_l$) and transverse ($v_t$) sound speed measured at room temperature. $C_v$ denotes heat capacity per unit volume determined by heat capacity under constant pressure $C_p$ and sample density $\rho$ via $C_v = C_p\rho$. The $l_{ph}$ varying with Nb content at 303 K is presented in Fig. 9(d). The $l_{ph}$ shows a continuous decline from ~ 7.74 Å for $Bi_6Cu_2Se_{3.6}Cl_{0.4}O_6$ to ~ 6.98 Å for $Bi_{5.895}Nb_{0.105}Cu_2Se_{3.6}Cl_{0.4}O_6$, decreased by 10%. The apparent decrease of $l_{ph}$ leads to the declining $\kappa_{lat}$, manifesting the intensed phonon scattering introduced by the point defects after Nb doping.

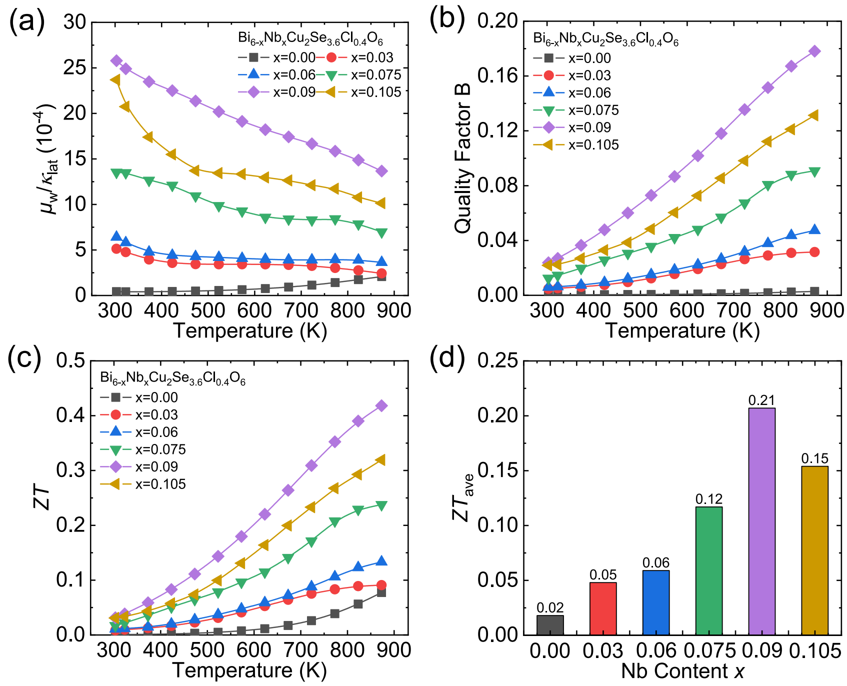


**Fig. 10.** Thermoelectric performance of $Bi_{6-x}Nb_xCu_2Se_{3.6}Cl_{0.4}O_6$ ($0 \leq x \leq 0.105$): temperature-dependent (a) the ratio of weighted carrier mobility to lattice thermal conductivity, (b) quality factor and (c) *ZT* values; (d) $ZT_{ave}$ from 303 K to 873 K in different Nb content.

To synthetically evaluate the role of Nb doped in Bi sites, the value of $\mu_w/\kappa_{lat}$ is quantified and plotted in Fig. 10(a). A sharply optimization can be observed over the entire temperature range after Nb substitution. A significantly improvement of ~ 660% is obtained in $Bi_{5.91}Nb_{0.09}Cu_2Se_{3.6}Cl_{0.4}O_6$ at 873 K. The boost of $\mu_w/\kappa_{lat}$ indicates that Nb substitution can intense the phonon scattering but concurrently promote electrons transport. The dimensionless quality factor *B*, which is proportional to the *ZT* value, can be quantified by $\mu_w/\kappa_{lat}$ via Eq. (12) [5,67]:

$$B = 9\frac{\mu_w}{\kappa_{lat}}\left(\frac{T}{300}\right)^{\frac{5}{2}} \tag{12}$$

As shown in Fig. 10(b), the quality factor *B* of each sample presents an upward trend varying with temperature, and possesses obvious enhancements after Nb substitution especially in high temperature range. The significant increase of *B* also implies the optimization of *ZT* value. Beneficial from the overall optimized electrical transport properties, although the $\kappa_{tot}$ is mildly increased, the *ZT* value over the entire temperature range is worthy of a remarkably increase. Ultimately, the maximal *ZT* value of ~ 0.4 is acquired in $Bi_{5.91}Nb_{0.09}Cu_2Se_{3.6}Cl_{0.4}O_6$ at 873 K, resulting in a ~ 450% enhancement compared with the $Bi_6Cu_2Se_{3.6}Cl_{0.4}O_6$ matrix (Fig. 10(c)). The $ZT_{ave}$ from 303 K to 873 K of $Bi_{6-x}Nb_xCu_2Se_{3.6}Cl_{0.4}O_6$ ($0 \leq x \leq 0.105$) is calculated via Eq. (13) and shown in Fig. 10(d):

$$ZT_{ave} = \frac{1}{T_h - T_c}\int_{T_c}^{T_h} ZT\,dT \tag{13}$$

where $T_h$ and $T_c$ express the hot-side temperature and the cold-side temperature, respectively. The max $ZT_{ave}$ of ~ 0.21 is acquired in $Bi_{5.91}Nb_{0.09}Cu_2Se_{3.6}Cl_{0.4}O_6$, enhanced by almost a factor of 10 as compared to the $Bi_6Cu_2Se_{3.6}Cl_{0.4}O_6$ matrix. It can be mainly attributed to the increase of carrier concentration and weak temperature dependence of resonance levels, which lead to the large increase of *PF* over the whole temperature region.

## 4. Conclusions

In summary, a new oxygen-containing *n*-type $Bi_6Cu_2Se_4O_6$-based TE materials with considerable thermoelectric performance were realized. The intrinsic low thermal conductivity of pristine $Bi_6Cu_2Se_4O_6$ can be attributed to the strong acoustic-optic coupling, soft phonon modes and strong anharmonicity, verified by DFT calculations. Based on Cl doping, Nb substitution at Bi sites not only increases the carrier concentration, but sustially enhances the effective mass by inducing resonant levels around Fermi level, leading to the overall enhancement of electrical properties, with a peak *PF* ~ 4.3 $\mu$V cm$^{-1}$ K$^{-2}$ at 873 K in $Bi_{5.91}Nb_{0.09}Cu_2Se_{3.6}Cl_{0.4}O_6$. Moreover, Nb doping can further reduce the lattice thermal conductivity, which is well reflected by the reduced phonon mean free path. Appearently, Nb substituent can intensely scatter phonons but concurrently promote electrons transport mainly by inducing the resonant states, reflecting the versatility of Nb doping in $Bi_6Cu_2Se_4O_6$. Finally, a maximal *ZT* ~ 0.4 at 873 K and an average *ZT* ~ 0.21 from 303 to 873 K are achieved in *n*-type $Bi_{5.91}Nb_{0.09}Cu_2Se_{3.6}Cl_{0.4}O_6$. This study broadens the applicability of resonant states to optimize thermoelectric performance as well as promotes the potential application of *n*-type $Bi_6Cu_2Se_4O_6$-based thermoelectric materials in medium temperature range, which is a remarkable achievement for *n*-type oxygen-containing thermoelectric materials.

## Declaration of Competing Interest

The authors declare no conflict of interest.

## Acknowledgments

This work was supported by the National Key Research and Development Program of China (2018YFA0702100 and 2018YFB0703600), National Natural Science Foundation of China (51772012), Beijing Natural Science Foundation (JQ18004) and National Postdoctoral Program for Innovative Talents

(BX20200028). L.D.Z. thanks for the support from the National Science Fund for Distinguished Young Scholars (51925101) and the high performance computing (HPC) resources at Beihang University.

## Supplementary materials

Supplementary material associated with this article can be found, in the online version, at doi:10.1016/j.actamat.2022.117930.

## References

[1] L.E. Bell, Cooling, heating, generating power, and recovering waste heat with thermoelectric systems, Science 321 (2008) 1457.
[2] L.-D. Zhao, J.Q. He, D. Berardan, Y.H. Lin, J.-F. Li, C.-W. Nan, N. Dragoe, BiCuSeO oxyselenides: new promising thermoelectric materials, Energy Environ. Sci. 7 (9) (2014) 2900–2924.
[3] X. Shi, L.D. Chen, Thermoelectric materials step up, Nat. Mater. 15 (7) (2016) 691–692.
[4] X.Y. Zhou, Y.C. Yan, X. Lu, H.T. Zhu, X.D. Han, G. Chen, Z.F. Ren, Routes for high-performance thermoelectric materials, Mater. Today 21 (9) (2018) 974–988.
[5] G.J. Tan, L.-D. Zhao, M.G. Kanatzidis, Rationally designing high-performance bulk thermoelectric materials, Chem. Rev. 116 (19) (2016) 12123–12149.
[6] B.C. Qin, D.Y. Wang, X.X. Liu, Y.X. Qin, J.-F. Dong, J.F. Luo, J. Li, W.-W. Liu, G.J. Tan, X.F. Tang, J.-F. Li, J.Q. He, L.-D. Zhao, Power generation and thermoelectric cooling enabled by momentum and energy multiband alignments, Science 373 (2021) 556–561.
[7] Y.-L. Pei, Y. Liu, Electrical and thermal transport properties of Pb-based chalcogenides: PbTe, PbSe, and PbS, J. Alloys Compd. 514 (2012) 40–44.
[8] Y. Xiao, D.Y. Wang, Y. Zhang, C.R. Chen, S.X. Zhang, K.D. Wang, G.T. Wang, S.J. Pennycook, G.J. Snyder, H.J. Wu, L.-D. Zhao, Band sharpening and band alignment enable high quality factor to enhance thermoelectric performance in *n*-type PbS, J. Am. Chem. Soc. 142 (8) (2020) 4051–4060.
[9] X. Qian, H.J. Wu, D.Y. Wang, Y. Zhang, J.F. Wang, G.T. Wang, L. Zheng, S.J. Pennycook, L.-D. Zhao, Synergistically optimizing interdependent thermoelectric parameters of *n*-type PbSe through alloying CdSe, Energy Environ. Sci. 12 (6) (2019) 1969–1978.
[10] Y. Xiao, D.Y. Wang, B.C. Qin, J.F. Wang, G.T. Wang, L.-D. Zhao, Approaching topological insulating states leads to high thermoelectric performance in *n*-type PbTe, J. Am. Chem. Soc. 140 (40) (2018) 13097–13102.
[11] Y. Jin, T. Hong, D.Y. Wang, Y. Xiao, W.K. He, X. Gao, Y.T. Qiu, L.-D. Zhao, Band structure and microstructure modulations enable high quality factor to elevate thermoelectric performance in $Ge_{0.9}Sb_{0.1}Te$-x%$FeTe_2$, Mater. Today Phys. 20 (2021) 100444.
[12] G.J. Tan, F.Y. Shi, S.Q. Hao, H. Chi, T.P. Bailey, L.-D. Zhao, C. Uher, C. Wolverton, V.P. Dravid, M.G. Kanatzidis, Valence band modification and high thermoelectric performance in SnTe heavily alloyed with MnTe, J. Am. Chem. Soc. 137 (35) (2015) 11507–11516.
[13] J. Androulakis, K.F. Hsu, R. Pcionek, H. Kong, C. Uher, J.J. D'Angelo, A. Downey, T. Hogan, M.G. Kanatzidis, Nanostructuring and high thermoelectric efficiency in *p*-type $Ag(Pb_{1-y}Sn_y)_mSbTe_{2+m}$, Adv. Mater. 18 (9) (2006) 1170–1173.
[14] X.Y. Liu, D.Y. Wang, H.J. Wu, J.F. Wang, Y. Zhang, G.T. Wang, S.J. Pennycook, L.-D. Zhao, Intrinsically low thermal conductivity in $BiSbSe_3$: a promising thermoelectric material with multiple conduction bands, Adv. Funct. Mater. 29 (3) (2019) 1806558.
[15] S.N. Wang, L.Z. Su, Y.T. Qiu, Y. Xiao, L.-D. Zhao, Enhanced thermoelectric performance in Cl-doped $BiSbSe_3$ with optimal carrier concentration and effective mass, J. Mater. Sci. Technol. 70 (2021) 67–72.
[16] X.X. Zhang, C. Chang, Y.M. Zhou, L.-D. Zhao, BiCuSeO thermoelectrics: an update on recent progress and perspective, Materials 10 (2) (2017) 198–213.
[17] J.Q. Zheng, D.Y. Wang, L.-D. Zhao, An update review on *n*-type layered oxyselenide thermoelectric materials, Materials 14 (14) (2021) 3905.
[18] N. Dragoe, Entropy driven synthesis of new materials, Mater. Lab. 1 (2002) 1–3.
[19] X.-L. Shi, H. Wu, Q.F. Liu, W. Zhou, S.Y. Lu, Z.P. Shao, M. Dargusch, Z.-G. Chen, $SrTiO_3$-based thermoelectrics: progress and challenges, Nano Energy 78 (2020) 105195.
[20] R. Shimonishi, M. Hagiwara, S. Fujihara, Fabrication of highly textured $Ca_3Co_4O_9$ ceramics with controlled density and high thermoelectric power factors, J. Eur. Ceram. Soc. 40 (4) (2020) 1338–1343.
[21] T.Y. Liu, D.Y. Bao, Y. Wang, H. Gao, D.L. Zhou, G. Han, J. Tang, Z.-Y. Huang, L. Yang, Z.-G. Chen, Exploring thermoelectric performance of $Ca_3Co_4O_{9+\delta}$ ceramics via chemical electroless plating with Cu, J. Alloys Compd. 821 (2020) 153522.
[22] B.B. Zhu, C. Chen, Z.C. Yao, J.Y. Chen, C. Jia, Z.H. Wang, R.M. Tian, L. Tao, F. Xue, H.H. Hng, Multiple doped ZnO with enhanced thermoelectric properties, J. Eur. Ceram. Soc. 41 (7) (2021) 4182–4188.
[23] H.J. Wu, L.L. Chen, S.T. Ning, X.D. Zhao, S.P. Deng, N. Qi, F. Ren, Z.Q. Chen, J. Tang, Extremely low thermal conductivity and enhanced thermoelectric performance of porous Gallium-doped $In_2O_3$, ACS Appl. Energy Mater. 4 (11) (2021) 12943–12953.
[24] A. Ahmad, M. Hussain, Z.F. Zhou, R. Liu, Y.-H. Lin, C.-W. Nan, Thermoelectric performance enhancement of vanadium doped *n*-type $In_2O_3$ ceramics via carrier engineering and phonon suppression, ACS Appl. Energy Mater. 3 (2) (2019) 1552–1558.
[25] Y. Liu, L.-D. Zhao, Y.C. Zhu, Y.C. Liu, F. Li, M.J. Yu, D.B. Liu, W. Xu, Y.-H. Lin, C.-W. Nan, Synergistically optimizing electrical and thermal transport properties of BiCuSeO via a dual-doping approach, Adv. Energy Mater. 6 (9) (2016) 1502423.
[26] X.X. Zhang, D. Feng, J.Q. He, L.D. Zhao, Attempting to realize *n*-type BiCuSeO, J. Solid State Chem. 258 (2018) 510–516.
[27] X.X. Zhang, D.Y. Wang, G.T. Wang, L.-D. Zhao, Realizing *n*-type BiCuSeO through halogens doping, Ceram. Int. 45 (12) (2019) 14953–14957.
[28] Q.D. Gibson, M.S. Dyer, C. Robertson, C. Delacotte, T.D. Manning, M.J. Pitcher, L.M. Daniels, M. Zanella, J. Alaria, J.B. Claridge, M.J. Rosseinsky, $Bi_{2+2n}O_{2+2n}Cu_{2-\delta}Se_{2+n-\delta}X_\delta$ (X = Cl, Br): a three-anion homologous series, Inorg. Chem. 57 (20) (2018) 12489–12500.
[29] X.X. Zhang, Y.T. Qiu, D.D. Ren, L.-D. Zhao, Electrical and thermal transport properties of *n*-type $Bi_6Cu_2Se_4O_6$ (2BiCuSeO + $2Bi_2O_2Se$), Ann. Phys. 532 (11) (2019) 1900340.
[30] J.Q. Zheng, D.Y. Wang, L.-D. Zhao, Enhancing thermoelectric performance of *n*-type $Bi_6Cu_2Se_4O_6$ through introducing transition metal elements, Scr. Mater. 202 (2021) 114010.
[31] J.P. Heremans, B. Wiendlocha, A.M. Chamoire, Resonant levels in bulk thermoelectric semiconductors, Energy Environ. Sci. 5 (2) (2012) 5510–5530.
[32] J.P. Heremans, V. Jovovic, E.S. Toberer, A. Saramat, K. Kurosaki, A. Charoenphakdee, S. Yamanaka, G.J. Snyder, Enhancement of thermoelectric efficiency in PbTe by distortion of the electronic density of states, Science 321 (2008) 554–557.
[33] B. Wiendlocha, Thermopower of thermoelectric materials with resonant levels: PbTe: Tl versus PbTe: Na and $Cu_{1-x}Ni_x$, Phys. Rev. B 97 (20) (2018) 205203.
[34] B. Wiendlocha, Fermi surface and electron dispersion of PbTe doped with resonant Tl impurity from KKR-CPA calculations, Phys. Rev. B 88 (20) (2013) 205205.
[35] C.M. Jaworski, B. Wiendlocha, V. Jovovic, J.P. Heremans, Combining alloy scattering of phonons and resonant electronic levels to reach a high thermoelectric figure of merit in PbTeSe and PbTeS alloys, Energy Environ. Sci. 4 (10) (2011) 4155–4162.
[36] Q. Zhang, B. Liao, Y. Lan, K. Lukas, W. Liu, K. Esfarjani, C. Opeil, D. Broido, G. Chen, Z. Ren, High thermoelectric performance by resonant dopant indium in nanostructured SnTe, Proc. Natl. Acad. Sci. U.S.A. 110 (33) (2013) 13261.
[37] S. Misra, B. Wiendlocha, J. Tobola, F. Fesquet, A. Dauscher, B. Lenoir, C. Candolfi, Band structure engineering in $Sn_{1.03}Te$ through an In-induced resonant level, J. Mater. Chem. C 8 (3) (2020) 977–988.
[38] L. Wu, X. Li, S. Wang, T. Zhang, J. Yang, W. Zhang, L. Chen, J. Yang, Resonant level-induced high thermoelectric response in indium-doped GeTe, NPG Asia Mater. 9 (1) (2017) e343.
[39] C.M. Jaworski, V. Kulbachinskii, J.P. Heremans, Resonant level formed by tin in $Bi_2Te_3$ and the enhancement of room-temperature thermoelectric power, Phys. Rev. B 80 (23) (2009) 233201.
[40] B. Wiendlocha, J.B. Vaney, C. Candolfi, A. Dauscher, B. Lenoir, J. Tobola, An Sn-induced resonant level in $\beta$-$As_2Te_3$, Phys. Chem. Chem. Phys. 20 (18) (2018) 12948–12957.
[41] M. Parzer, F. Garmroudi, A. Riss, S. Khmelevskyi, T. Mori, E. Bauer, High solubility of Al and enhanced thermoelectric performance due to resonant states in $Fe_2VAl_x$, Appl. Phys. Lett. 120 (7) (2022) 071901.
[42] J.W. Simonson, D. Wu, W.J. Xie, T.M. Tritt, S.J. Poon, Introduction of resonant states and enhancement of thermoelectric properties in half-Heusler alloys, Phys. Rev. B 83 (23) (2011) 235211.
[43] X. Tan, J.L. Lan, G. Ren, Y. Liu, C.-W. Nan, Enhanced thermoelectric performance of *n*-type $Bi_2O_2Se$ by Cl-doping at Se site, J. Am. Ceram. Soc. 98 (2017) 1494–1501.
[44] D.T. Morelli, V. Jovovic, J.P. Heremans, Intrinsically minimal thermal conductivity in cubic I-V-$VI_2$ semiconductors, Phys. Rev. Lett. 101 (3) (2008) 035901.
[45] Y.S. Zhang, E. Skoug, J. Cain, V. Ozoliņš, D. Morelli, C. Wolverton, First-principles description of anomalously low lattice thermal conductivity in thermoelectric Cu-Sb-Se ternary semiconductors, Phys. Rev. B 85 (5) (2012) 054306.
[46] M. Samanta, K. Pal, P. Pal, U.V. Waghmare, K. Biswas, Localized vibrations of Bi bilayer leading to ultralow lattice thermal conductivity and high thermoelectric performance in weak topological insulator *n*-type BiSe, J. Am. Chem. Soc. 140 (17) (2018) 5866–5872.
[47] B.C. Qin, D.Y. Wang, L.-D. Zhao, Slowing down the heat in thermoelectrics, InfoMat 3 (7) (2021) 755–789.
[48] D.Y. Wang, Z.W. Huang, Y. Zhang, L.J. Hao, G.T. Wang, S.H. Deng, H.L. Wang, J. Chen, L.H. He, B. Xiao, Y.D. Xu, S.J. Pennycook, H.J. Wu, L.-D. Zhao, Extremely low thermal conductivity from bismuth selenohalides with 1D soft crystal structure, Sci. China Mater. 63 (9) (2020) 1759–1768.
[49] L.-D. Zhao, S.H. Lo, Y. Zhang, H. Sun, G. Tan, C. Uher, C. Wolverton, V.P. Dravid, M.G. Kanatzidis, Ultralow thermal conductivity and high thermoelectric figure of merit in SnSe crystals, Nature 508 (7496) (2014) 373–377.
[50] J.Y. Cho, X. Shi, J.R. Salvador, G.P. Meisner, J. Yang, H. Wang, A.A. Wereszczak, X. Zhou, C. Uher, Thermoelectric properties and investigations of low thermal conductivity in Ga-doped $Cu_2GeSe_3$, Phys. Rev. B 84 (8) (2011) 085207.
[51] Y.-L. Pei, J.Q. He, J.-F. Li, F. Li, Q.J. Liu, W. Pan, C. Barreteau, D. Berardan, N. Dragoe, L.D. Zhao, High thermoelectric performance of oxyselenides: intrinsically low thermal conductivity of Ca-doped BiCuSeO, NPG Asia Mater. 5 (5) (2013) e47.

[52] K. Kurosaki, A. Kosuga, H. Muta, M. Uno, S. Yamanaka, $Ag_9TlTe_5$: a high-performance thermoelectric bulk material with extremely low thermal conductivity, Appl. Phys. Lett. 87 (6) (2005) 061919.
[53] C.L. Wan, W. Pan, Q. Xu, Y.X. Qin, J.D. Wang, Z.X. Qu, M.H. Fang, Effect of point defects on the thermal transport properties of$(La_xGd_{1-x})_2Zr_2O_7$: experiment and theoretical model, Phys. Rev. B 74 (14) (2006) 144109.
[54] G.J. Snyder, E.S. Toberer, Complex thermoelectric materials, Nat. Mater. 7 (2) (2008) 105–114.
[55] B. Qin, L.-D. Zhao, Carriers: the Less, the Faster, Mater. Lab. 1 (2022) 1–3.
[56] J.S. Cha, D.H. Kim, H.Y. Hong, K. Park, Enhanced thermoelectric performance of spark plasma sintered p-type $Ca_{3-x}Y_xCo_4O_{9+\delta}$ systems, J. Mater. Sci. Tech. 55 (2020) 212–222.
[57] D.H. Kim, H.Y. Hong, J.K. Lee, S.D. Park, K. Park, Crystal structure and thermoelectric transport properties of Cu−deficient BiCuSeO oxyselenides, J. Mater. Res. Tech. 9 (6) (2020) 16202–16213.
[58] H.Y. Hong, D.H. Kim, S.O. Won, K. Park, Enhancement of the thermoelectric performance of $n$−type $Bi_2O_2Se$ by $Ce^{4+}$ doping, J. Mater. Res. Tech. 15 (2021) 4161–4172.
[59] J.W. Seo, G.H. Kim, S.M. Choi, K. Park, High-temperature thermoelectric properties of polycrystalline $CaMn_{1-x}Nb_xO_{3-\delta}$, Ceram. Int. 44 (8) (2018) 9204–9214.
[60] C.M. Kim, D.H. Kim, H.Y. Hong, K. Park, Thermoelectric properties of $La^{3+}$ and $Ce^{3+}$ co-doped $CaMnO_3$ prepared by tape casting, J. Eur. Ceram. Soc. 40 (3) (2020) 735–741.
[61] D.H. Kim, H.Y. Hong, K. Park, High thermoelectric properties of $p$-type BiCuSeO co−doped with $Ca^{2+}$ and $Ba^{2+}$, J. Alloys Compd. 876 (2021) 159969.
[62] Y. Xiao, H. Wu, W. Li, M. Yin, Y. Pei, Y. Zhang, L. Fu, Y. Chen, S.J. Pennycook, L. Huang, J. He, L.-D. Zhao, Remarkable roles of Cu to synergistically optimize phonon and carrier transport in $n$-Type PbTe-$Cu_2Te$, J. Am. Chem. Soc. 139 (51) (2017) 18732–18738.
[63] D.L. Dexter, F. Seitz, Effects of dislocations on mobilities in semiconductors, Phys. Rev. 86 (6) (1952) 964–965.
[64] S.D. Kang, G.J. Snyder, Charge-transport model for conducting polymers, Nat. Mater. 16 (2) (2017) 252–257.
[65] Y. Xiao, H.J. Wu, J. Cui, D.Y. Wang, L.W. Fu, Y. Zhang, Y. Chen, J.Q. He, S.J. Pennycook, L.-D. Zhao, Realizing high performance $n$-type PbTe by synergistically optimizing effective mass and carrier mobility and suppressing bipolar thermal conductivity, Energy Environ. Sci. 11 (9) (2018) 2486–2495.
[66] G.J. Snyder, A.H. Snyder, M. Wood, R. Gurunathan, B.H. Snyder, C. Niu, Weighted mobility, Adv. Mater. 32 (25) (2020) e2001537.
[67] R.P. Chasmar, R. Stratton, The thermoelectric figure of merit and its relation to thermoelectric generators, J. Electron. Control 7 (1) (1959) 52–72.
[68] G. Tan, F. Shi, H. Sun, L.-D. Zhao, C. Uher, V.P. Dravid, M.G. Kanatzidis, SnTe–$AgBiTe_2$ as an efficient thermoelectric material with low thermal conductivity, J. Mater. Chem. A 2 (48) (2014) 20849–20854.
[69] M. Zhao, C. Chang, Y. Xiao, L.-D. Zhao, High performance of n-type $(PbS)_{1-x-y}(PbSe)_x(PbTe)_y$ thermoelectric materials, J. Alloys Compd. 744 (2018) 769–777.
[70] Y. Xiao, W. Li, C. Chang, Y. Chen, L. Huang, J. He, L.-D. Zhao, Synergistically optimizing thermoelectric transport properties of $n$-type PbTe via Se and Sn co-alloying, J. Alloys Compd. 724 (2017) 208–221.
[71] X. Tan, Y.C. Liu, R. Liu, Z.F. Zhou, C. Liu, J.L. Lan, Q.H. Zhang, Y.-H. Lin, C.-W. Nan, Synergistical enhancement of thermoelectric properties in $n$-type $Bi_2O_2Se$ by carrier engineering and hierarchical microstructure, Adv. Energy Mater. 9 (31) (2019) 1900354.